Usage of Body-Fitted Windows in PIV Image Processing

Matthew Ward*, Adrian Spencer, Martin Passmore

Aeronautical and Automotive Engineering Department, Loughborough University

* Correspondent author: M.Ward2@lboro.ac.uk

Keywords: PIV processing, Interrogation windows, Body fitted

ABSTRACT

Flow close to the boundaries of bodies is often difficult to measure using particle image velocimetry (PIV); factors such as glare, velocity gradients and the body itself all present challenges in obtaining good quality results. One common problem in conventional PIV algorithms is that they are based on square grids, which for most applications is not aligned with the shape of the body. This means the body will clip part of the window resulting in fewer particles and erroneously placed vectors.

Being able to align the interrogation window shape to the body boundary would remove these sources of error. This study investigates the effect that applying non-square windows has, compared to conventional square windows for three test cases: a free-field, a circular body and an airfoil shape. For each of these a number of interrogation methods are tested.

For the circular body, conventional and rotated square windows were tested along with a body fitted mesh. The image was also deformed into R-θ coordinates to enable conventional square window processing, before de-warping the vector field. Square, rotated square and body fitted techniques were also tested on an airfoil shape. It was found that the body-fitted and warping methods both showed significant improvements in the boundary layer over the square meshes; although the warping process added computational expense. The meshing technique was found to have little impact on the free field as there was no body or velocity gradient.

Utilising this interrogation method in conjunction with developed methods of automated edge detection and more mature processing algorithms will result in better measurements close to bodies than is possible with conventional square windows. An example application of this technique on flow around a sphere is also demonstrated.

1 Introduction

Achieving good quality PIV measurements close to boundaries is difficult to achieve, but is important as it often reveals important features of the flow. Ordinarily, in the presence of a curved or sloped boundary, there are issues such as local glare obscuring particles and smearing correlation peaks, or non-planar reflections illuminating out-of-plane particles (Theunissen, Scarano, & Riethmuller, 2008). This will influence the likelihood of detecting the correlation peak and its accuracy.

One of the motives behind this work is to reliably identify the instantaneous separation point around a spherical body; this usually requires some intelligent extrapolation from the reliable vector field to the body boundary.

One way to avoid this requirement for extrapolation, is to distort or transform the image into more rectangular-friendly coordinates (Park, Im, Sung, & Park, 2015), but the issue here is that the image distortion is computationally expensive and the errors introduced can outweigh any gains in resolution close to boundaries (Masullo & Theunissen, 2017; T. D. Nguyen, Wells, & Nguyen, 2012).

Areas of high velocity gradients can also introduce errors (Huang, Fiedler, & Wang, 1993a) and can be analysed using this method as the window shapes and sizes can be tailored to the flow field. This could be used in addition to local image deformation techniques such as those described by Huang, Fiedler, & Wang (1993b); Jambunathan, Ju, Dobbins, & Ashforth-Frost, (1999) and Nogueira & Lecuona, (2004). These authors deform the search particle image pattern (SPIP) to reduce the errors in correlation that these flow features introduce. This procedure is undertaken as a second pass after conventional PIV techniques are able to provide a first estimate of the velocity and velocity gradients. This will (possibly after multiple iterations) result in much more uniform particle shifts across the window, resulting in a stronger correlation. Translation of the SPIP is also used to reduce the magnitude of this particle shift (Scarano & Riethmuller, 1999; Wenguo, Fan, Liao, & Qin, 2001). These sources demonstrate that particle shifts closer to zero are more accurate. Whilst these methods are useful to reduce the errors which can be associated with velocity gradients, they still suffer from effects such as glare, window clipping and erroneously placed velocity vectors.

It has been demonstrated that it is possible to reduce reflections in the experimental phase by using surface treatments (Paterna, Moonen, Dorer, & Carmeliet, 2013) and in image pre-processing by using various techniques (Deen et al., 2010; Mendez et al., 2017). Whilst these methods have been shown to give some improvement to the raw images, it does not resolve the inherent problems of applying a Cartesian based windowing approach to curved surfaces.

One approach to overcome this problem is to mask out the body, leaving only 'good' data to use in the cross-correlation or Fast Fourier Transform (FFT) procedure (Ronneberger, Raffel, & Kompenhans, 1998). This approach results in an arbitrarily shaped window, with no surface glare interfering with the results, which improves the correlations and hence results close to the boundary. However, there is little control over the resultant window size; which can mean that the window close to the boundary is not large enough to capture sufficient particles for an effective correlation; still not ensuring that the flow-field near the boundary can be effectively calculated. It will also place any calculated vector at the centre of the interrogation cell even though this may not be the centre of the valid flow area within the interrogation cell.

It is therefore desirable to introduce methods of more reliably generating vectors close to boundaries that are able to resolve high velocity gradients and cope with errors associated with

boundaries such as reflections and incomplete interrogation windows. To achieve this, a method has been developed to generate an initial mesh that can be body fitted or tailored to best suit the local velocity field and then undertake standard PIV procedures on these mesh cells. In general, this will require prior knowledge of the flow field to ensure that the mesh that is used is suitable for the flow.

Significant work has been undertaken on automated boundary or edge detection, both in the broader sense (Canny, 1986) and directly applied to PIV (Dussol, Druault, Mallat, Delacroix, & Germain, 2016; Masullo & Theunissen, 2017a). Body fitted meshing algorithms are also well developed. These methods can be used to locate the boundary effectively and generate a high quality, body-fitted mesh.

This procedure can be used in isolation across the whole image, or as a refinement method in regions where standard Cartesian windows are less effective due to boundaries or velocity gradients; prior knowledge of the flow field may be required to determine which is better suited to a particular application.

2   Processing Procedure

2.1   Mesh Generation

The mesh can be generated by the user externally to the PIV algorithm; the cells can be of any shape dictated by a list of Cartesian coordinates enabling pseudo-curves and multi-sided polygons. These coordinates are stored with the cell centroid and connectivity information for use later in the algorithm. It would be expected that one edge of the body-fitted mesh would be aligned to the most conservative edge of any glare present in the image pair.

To generate the body-fitted meshes used in the examples later in Sections 6 and 7, the profile of the body, ideal window height and width and overlap were passed to the mesh generation algorithm. This works along the profile until the width of the cell at its centroid is within an accepted tolerance of the desired width; this gives the bottom-most coordinates. The upper-most coordinates are placed at a distance equal to the desired height normal to the wall. The nearest profile point to the desired overlap is used as the starting point for the next cell and so on until the entire profile has been covered. The process is then repeated at the required height above the body to give the required overlap in the wall-normal direction. If multi-sided polygons are required (for example following curvature) points can be added to each cell as it is generated.

Mesh sensitivity analyses have not been undertaken for these tests, the aim was to keep the cell dimensions consistent with the square meshes. More intelligent meshing methods are also well developed and can be used as long as the cell size can be adequately controlled.

2.2   Window Preparation

For each cell of the mesh, the interrogation particle image pattern (IPIP) from the first image of the pair is constructed from the pixels that lie within the specified mesh cell boundaries. This is then padded with zero intensity values to form a rectangular window (see Figure 1). The SPIP is created from the same pixels as the padded IPIP from the second image of the pair (see Figure 2). The IPIP is padded with NaN values which do not bias the resulting correlation as zero padding (Adrian & Westerweel, 2011, pp. 372).

The figures below use hollow and solid dots to resemble the A and B images from the pair respectively. The solid red line in Figure 1 is the edge of the mesh cell and the dashed line in Figure 2 is for reference only. The cell can be of any shape to match the curvature of the body.

Whilst this padding is somewhat arbitrary (ideally just large enough to capture the motion of all the particles in the mesh cell), it is feasible to pad the window to the next 2^n size, which will enable a FFT to be undertaken, rather than using a direct cross-correlation technique. This is a similar concept to that suggested by Gui & Merzkirch (1998).
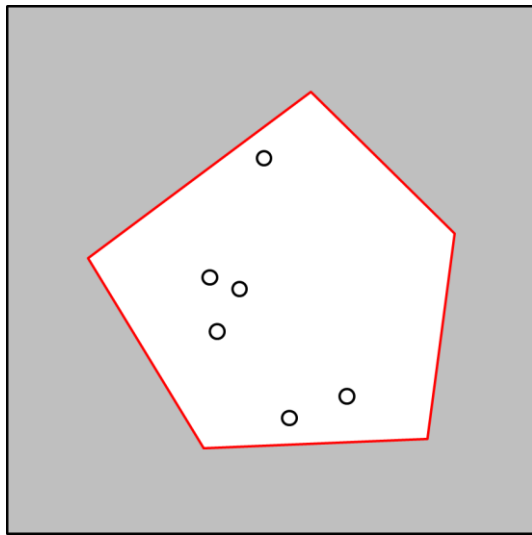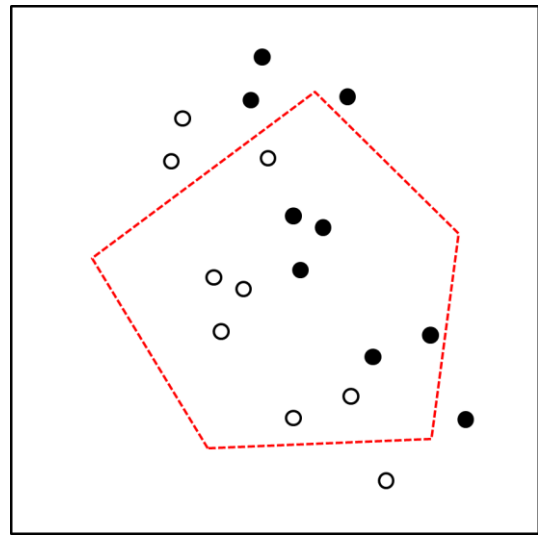

Figure 1: Masked IPIP

Figure 2: Matched SPIP

2.3   Cross-Correlation

In this case, a direct cross-correlation has been undertaken between the two windows, that will result in the calculation of a correlation field with potentially a number of peaks. For the vector to be valid the highest peak must be 'significantly' larger than the second highest (Adrian & Westerweel, 2011, pp. 343) – this 'significant' ratio is a user-defined threshold. If the peak ratio is below this value, the vector is discarded.

The velocity vector returned here is the average X and Y shift of the mesh cell, so the vector should be placed at the mesh cell centroid coordinates.

The cross-correlation routine will only return an integer pixel shift distance, which is not realistic. To estimate the shift to sub-pixel accuracy, a Gaussian fitted maximisation function is undertaken on the correlation field (Adrian & Westerweel, 2011, pp. 375).

2.4 Vector Validation

Once velocity vectors have been calculated for each mesh cell, it is important to remove any spurious, or false, vectors that can arise from erroneous correlation peaks. This is checked by comparing the vector in question to its immediate neighbours. The local median test described by Westerweel (1994) is used in this algorithm. The vector must be close to the median value of its immediate neighbours, within a tolerance based on the neighbours' standard deviation.

For a structured mesh, such as a rectangular or polar mesh, finding the neighbours is trivial, but less so for an unstructured or irregular mesh; to determine this, either the mesh connectivity is required or the nearest cells can be used.

2.5 Multi-Pass

A multi-pass algorithm is used in line with the WIDIM (WIndow Displacement Iterative Multigrid) method proposed by Scarano & Riethmuller (1999).

In this method, the SPIP is created from the pixels one shift away from the IPIP, such that the post-shift particles should lie on top of each other, aside from velocity gradients and vorticity. This shift value is taken from the median of the neighbours as described in the previous section.

This reduces the impact of errors introduced by larger pixel displacements, as demonstrated in the same paper. A second cross-correlation is then performed. Extra confidence can be taken in a correlation peak around zero, which can be used to validate vectors which would have failed the initial peak ratio test.

To account for inhomogeneous particle shifts within a mesh cell, deformation techniques as described earlier in the paper can be used (although are not utilised in this algorithm). This will improve the strength of the correlation peak as all particles in the cell should now move with a more consistent velocity vector.

The spurious detection and multi-pass algorithms can be run several times to maximise the number and improve the accuracy of valid vectors.

2.6   Interpolation

It is likely that there will still be cells where it is not possible to detect a valid velocity vector, perhaps due to an inability to detect a valid correlation peak or for it to be marked as erroneous, even after multiple passes. 2D linear interpolations were undertaken to fill the gaps in the data. For the free field images (see Section 3), approximately 1% of vectors were populated in this way.

2.7   Limitations

It is well understood that this algorithm is not as well refined or complex as current best practices. It should be borne in mind that this paper aims to isolate the impact of manipulating the shapes and sizes of the interrogation windows; rather than absolute maturity and accuracy of the PIV algorithm itself.

3   Image Generation

All of the image pairs used in these tests are synthetic, which will enable the true velocity field to be known - enabling direct comparisons between the various PIV measured outputs and the true value. The first synthetic image of each pair is generated by randomly scattering particles across the image and the second by translating the particles by a known velocity field.

Three sets of synthetic images were generated: A free flow with constant velocity; a circular body with boundary layer and an airfoil shape with a boundary layer. The boundary layers are predicted using a power law (Munson, Okiishi, Huebsch, & Rothmayer, 2013) and are blended into the free stream. The airfoil is based on a NACA0012 shape (NASA & Rumsey, 2018) with a rounded trailing edge to enable effective meshing. Sample inverted images of each are shown in Figure 3 to Figure 5. The red and blue lines indicate the body and boundary layer edges respectively.
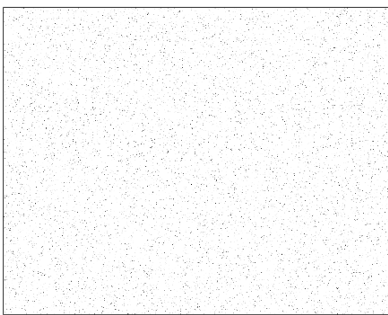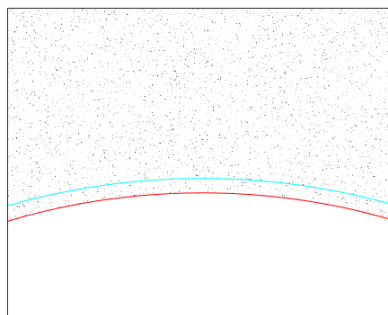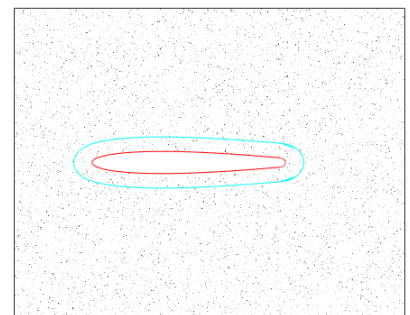

Figure 3: Free field   **Figure 4: Circular body**   **Figure 5: Airfoil body**

——————— Body boundary   ——————— Boundary layer edge

4   Error Calculations

The error for each cell was calculated using equation (1)

$$E = \frac{\sqrt{(X - X_t)^2 + (Y - Y_t)^2}}{\sqrt{(X_t)^2 + (Y_t)^2}} * 100\% \tag{1}$$

where: X and Y are the average measured pixel shifts in each cell and X_t and Y_t are the true shifts at the window centroid known from the synthetic image generation. In the results sections, the mean and 95th percentile confidence interval error values (as specified by Equation 2) are presented

$$CI_{95} = 1.96 * \frac{\sigma}{\sqrt{N}} \tag{2}$$

where: σ is the standard deviation of the sample and N is the number of samples.

To demonstrate the general accuracy of the PIV processing algorithm described above, the algorithm was tested on a set of 'free field' images. This used processing parameters of: 32x32 pixel windows, 50% overlap, two additional passes and linear interpolation, as described in section 2. The resulting error across the image was 0.67±0.01%.

5   Free-flow images

For the free flow images, a variety of square, rectangular and rotated rectangular windows are used to test if aligning the window with the direction of flow reduces the error. The square windows are 32x32 pixels, the rectangular windows are 45x22 pixels in width and length respectively and the rotated windows are the same size, but aligned with the flow vector at 12.5° from horizontal. The quantitative error values for each of these methods can be found in Table 1.

Table 1: Quantitative error values for the free field images

Mesh type	No. vectors	Average error (%)	CPU time per vector (ms)
Square (32x32)	8372	0.67±0.01	4.37
Rotated Square	8371	0.69±0.01	4.29
Rectangle (45x22)	5366	0.72±0.01	3.97
Rotated Rectangle	5080	0.72±0.01	4.98

Changing the size and orientation of the cells had little effect on the results. This was expected as the flow is uniform and there are sufficient particles in each window such that gaining or losing

particles from the windows is not significantly affecting the correlation procedure. If there were velocity gradients in the flow or sparse particles, then being able to manipulate the window shape and size can be used to reduce their impact. As an example, Meinhart, Wereley, & Santiago (1999) reduced the errors due to a velocity gradient by using high aspect ratio rectangular cells with the short edge parallel to the gradient.

6   Circular body

A set of images using the 'circular body' as described in Section 3 has been analysed using the square (Figure 6) and rotated square (Figure 7) windowing methods defined in section 5. A body fitted mesh (Figure 8) has also been tested. It has been demonstrated that warping the image for flow around bodies with simple or constant curvature produces effective results in reducing effects of surfaces (C. V. Nguyen, Nguyen, Wells, & Nakayama, 2010); although it incurs computational expense to perform the image warping and de-warping processes. This has also been tested here using the processing algorithm described, to compare result accuracy and computational expense. This result can be found in Figure 9.

Table 2 compares the errors and processing times for the various methods described in this section. The 'boundary layer error' value is the average error within the boundary layer specified in section 3 and shown using a blue line.

Table 2: Quantitative error values for tests on the circualr body

Mesh type	No. vectors	Average error (%)	Average boundary layer error (%)	CPU time per vector (ms)
Square	8372	1.03±0.04	4.82±0.12	3.50
Rotated Square	8371	0.91±0.02	4.21±0.06	3.03
Body fitted	5366	0.82±0.01	2.05±0.03	4.24
Warped Image	5080	1.08±0.01	2.64±0.03	9.31

It can be seen from the results in Table 2 that the average error across the image for each of the windowing methods remains largely similar, although there are some differences. The error within the boundary layer, however, decreases by over 50% by using the body fitted compared to the square windowing methods. The average error for the warped image is also lower, but takes significantly more time due to the image warping and de-warping processes.
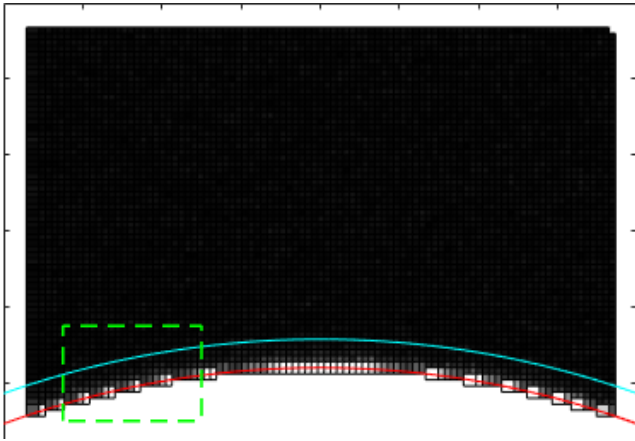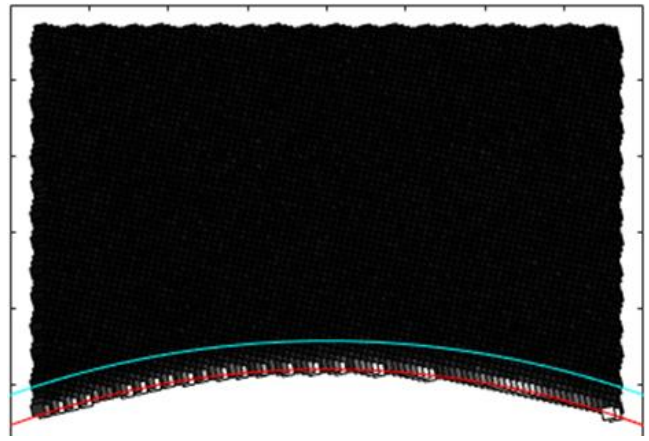
Figure 6: Circular body, square windows

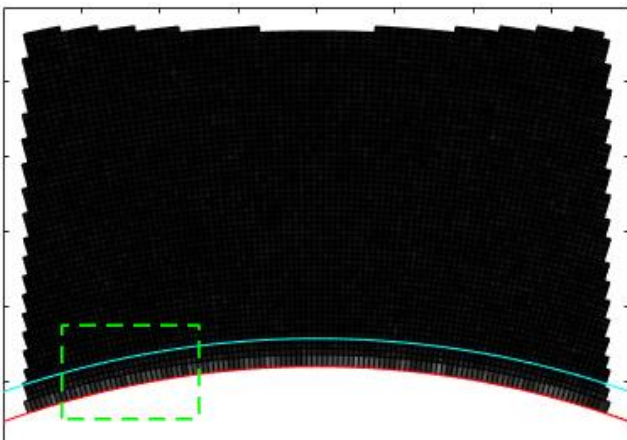**Figure 7: Circular body, rotated square windows**

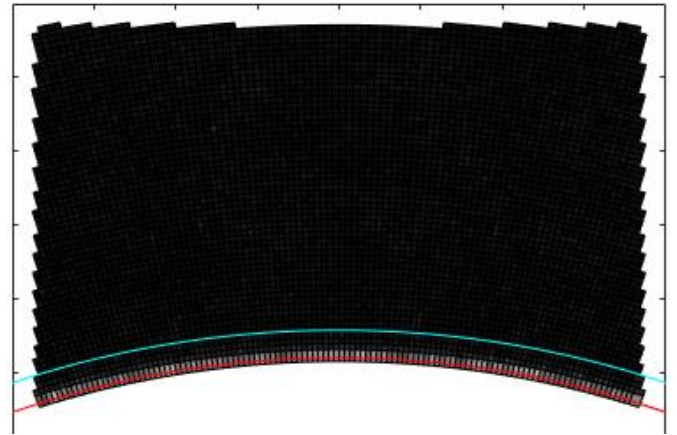**Figure 8: Circular body, body fitted windows**
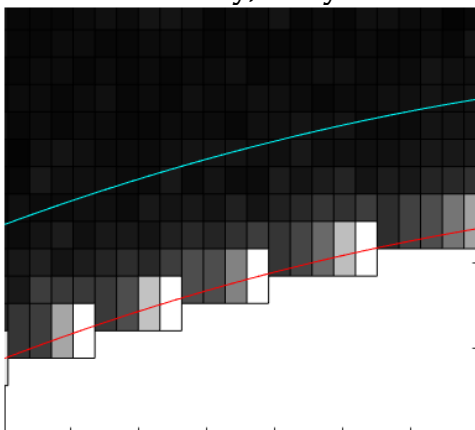

Figure 9: Circular body, warped image
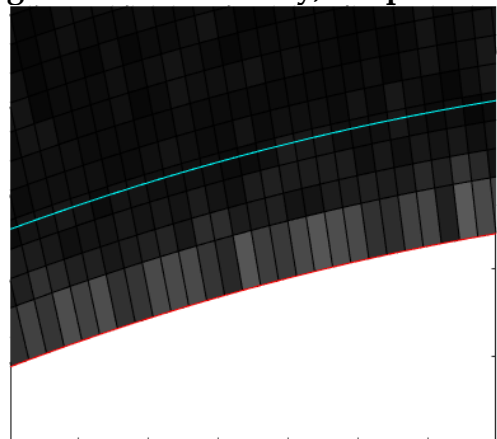

Figure 10: Circular body, square windows - magnified

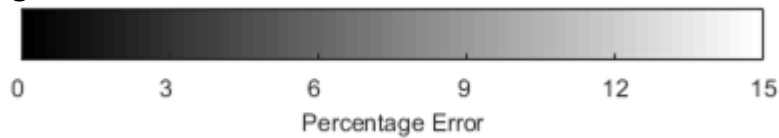
Figure 11: Circular body, body fitted windows - magnified

Percentage Error

Figure 10 and Figure 11 show magnified sections of the error maps using the square and body-fitted methods respectively. These images show that the highest errors appear in the cells where there is greatest overlap with the body.

One cause of error is that clipping the window reduces the number of particles in the window; which will in turn reduce the likelihood of gaining an effective correlation peak. Another cause is that the velocity vector of a clipped cell will be calculated from the valid region only, but the vector itself will be placed at the centroid of the entire cell. This is shown in Figure 12; the blue arrow is the more accurate velocity at the centroid of the valid region, the black is at the cell centroid. This error will not occur for the body fitted methods as there are no clipped cells.
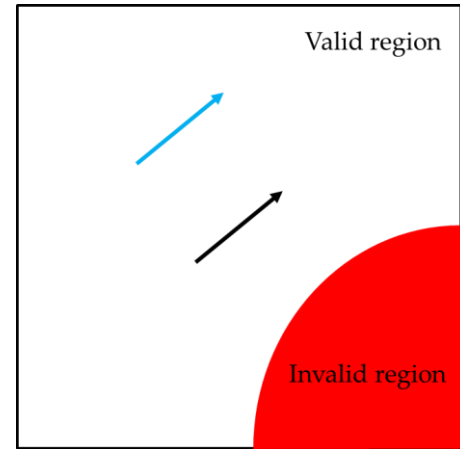

Figure 12: Errors due to incorrectly placed velocity vectors

Another potential source of improvement the body fitted windows provide is that the centroids of the cells are a constant perpendicular distance from the body boundary. This can assist with detecting separation and recirculation points in the wall-parallel velocity, as the wall-parallel velocity value is not contaminated by the wall-normal boundary layer gradient.

7 Airfoil shape

This technique is not limited to a simple circular body; any window cell shape can be used to improve measurements close to a body boundary. To demonstrate this, a NACA0012 wing shape has been selected (NASA & Rumsey, 2018) and the trailing edge rounded. The curvature is non-constant and, in particular at the leading and trailing edges, is quite sharp.

Square, rotated square and body fitted meshes were tested on the airfoil body; the results are reported in Figure 13 to Figure 15. Quantitative error values can be found in Table 3.

Table 3: Quantitative error values for tests on the airfoil body

Mesh type	No. vectors	Average error (%)	Average boundary layer error (%)	CPU time per vector (ms)
Square	8093	0.96±0.02	4.79±0.07	4.55
Rotated Square	8097	1.02±0.02	5.44±0.08	4.89
Body fitted	8594	0.96±0.01	3.86±0.04	5.26

As for the circular body, the average errors across the image are reasonably consistent; but the boundary layer error for the body fitted image has decreased. The error maps show that in all cases the largest errors are around the regions of highest curvature, which will also be the location of largest velocity gradient.

A warped airfoil image has not been tested in this study, but Masullo & Theunissen (2017) found that the image warping procedures were ineffective in regions of greater curvature, such as the leading and trailing edges of the wing. This is due to excessive stretching or compressing of the pixels, introducing additional errors. They also found that the results were sensitive to the generated mesh; this has not been studied in depth here.
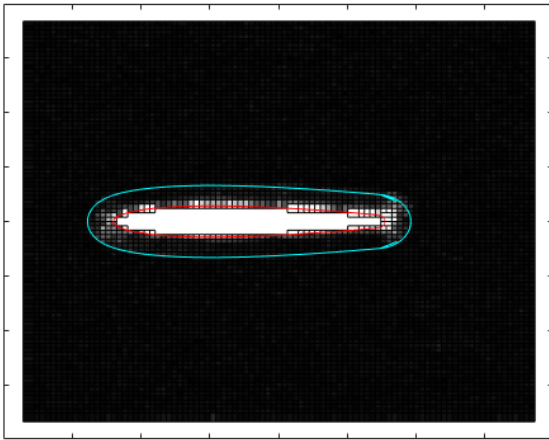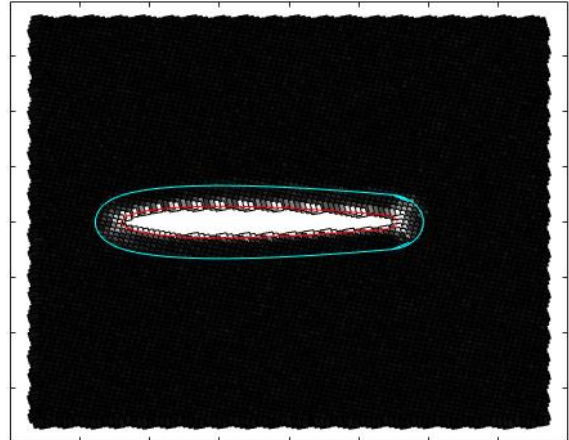
Figure 13: Airoil, square windows
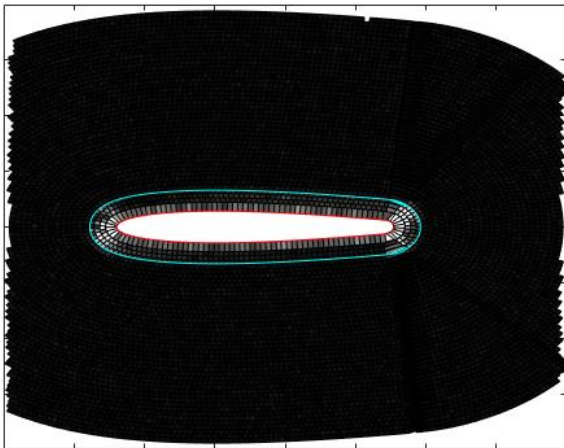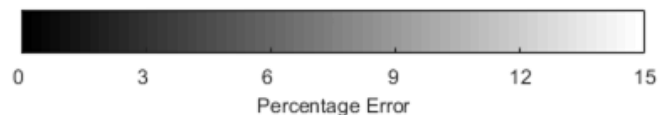
Figure 14: Airfoil, rotated square windows

Figure 15: Airfoil, body fitted windows

8   Example Application - Flow around a sphere

The motivation behind this work is to obtain better results in the boundary layer around non-square objects, in particular the flow around spheres. One of the key factors behind the flow field around a sphere is the separation location of the boundary layer, which can be estimated by

examining the wall-tangential velocity. With conventional PIV windowing techniques, this would require a method of removing the wall-normal gradient due to the boundary layer. With the body fitted windowing methods described here, the distance from the wall of the nearest vector is constant, removing the wall-normal gradient; as well as the improvement in accuracy as demonstrated previously in this article.

Figure 16 and Figure 17 show the resulting vector field from analysing real PIV images of flow around a sphere using square and body fitted windows respectively; Figure 18 and Figure 19 show the dashed green areas magnified. There is a shadow cast by the sphere, which prevents effective PIV measurement behind it. The red line indicates the body and edge of shadow.

10 image pairs were processed using the methods described in Section 2, but do not use interpolation to replace poor quality vectors (see Section 2.6). It can be seen from these images that the body-fitted windowing methods allows for the calculation of vectors much closer to the wall than using square windows, allowing more accurate estimation of the separation location.
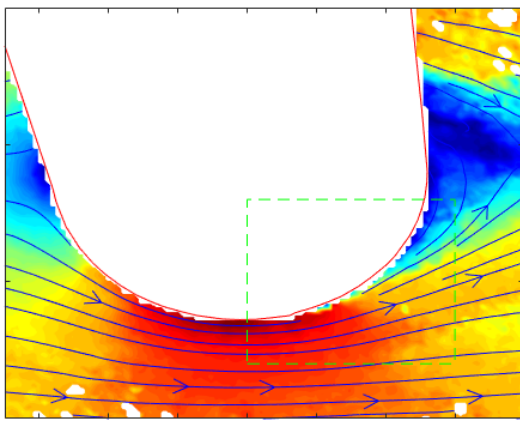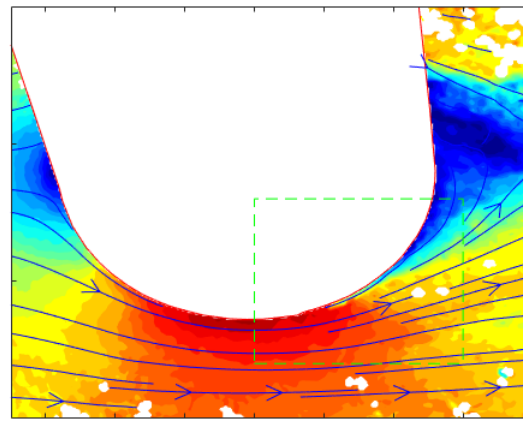

Figure 16: Square windows - real image

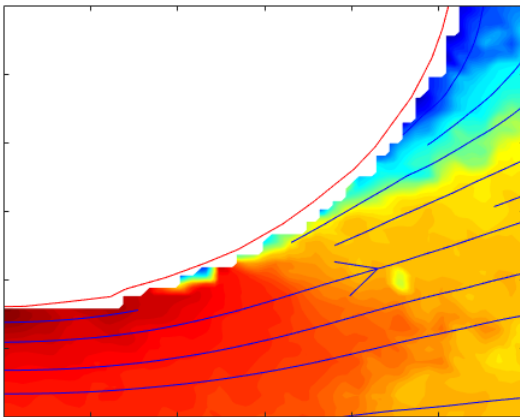**Figure 17: Body fitted windows - real image**

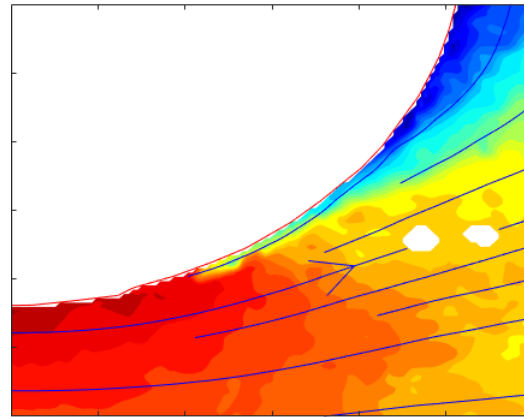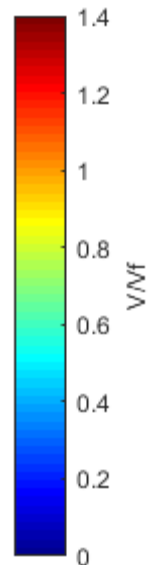**Figure 18: Square windows - real image - magnified**

Figure 19: Body fitted windows - real image - magnified

9   Conclusions

Methods of using non-square windows for PIV analysis have been examined. Four windowing methods were considered for use on three synthetically generated test cases: a free velocity field; a circular body and an airfoil shape. Conventional square windows, rotated square windows, body fitted windows and warped images were tested to determine if utilising more intelligent windowing techniques can reduce the errors associated with the body boundary.

Using cells that are fitted to a body resulted in reduced errors close to the body boundary compared to the conventional and rotated square windows. This reduction will be useful to enable much more effective near wall flow resolution, which is often problematic in PIV analysis. It is thought that these improvements arise for three reasons, firstly that not clipping the window will result in more particles being present in the interrogation region, thereby improving the likelihood of obtaining an accurate correlation peak; secondly the vector will be placed at the centroid of the window, not necessarily the centroid of the area the vector is computed from.

Warping the image into wall-parallel and wall-perpendicular coordinates, then undertaking conventional square window PIV also showed an improvement in accuracy near the wall; but at significant additional computational expense. Previous studies have also indicated that this methodology is less effective in regions of high curvature, which were not explicitly tested.

This investigation has shown an improvement on a small number of test cases, with high quality synthetic images and a relatively undeveloped PIV processing algorithm when compared to current best practices. It has also been used in an example application to locate the separation location on flow around a sphere. The next stage of work is to test this meshing methodology more thoroughly on more complex geometries with features such as glare and non-uniform particle distribution. If these benefits can still be seen on larger scale tests, this will enable much more effective measurements of near wall flow, particularly around objects with curvature.

Nomenclature

Abbreviation	In full	Abbr.	In full
DCC	Direct Cross-Correlation	E	Error
FFT	Fast Fourier Transform	N	Number of samples
IPIP	Interrogation Particle Image Pattern	X	Average pixel shift in X
NaN	Not a Number	X_t	True pixel shift in X
PIV	Particle Image Velocimetry	Y	Average pixel shift in Y
SPIP	Search Particle Image Pattern	Y_t	True pixel shift in Y
WIDIM	WIndow Displacement Iterative Multigrid	σ	Standard deviation

References

Adrian, R. J., & Westerweel, J. (2011). *Particle Image Velocimetry*. Cambridge, NY: Cambridge University Press.

Canny, J. (1986). A Computational Approach to Edge Detection. *IEEE Transactions on Pattern Analysis and Machine Intelligence*, *PAMI-8*(6), 679–698. https://doi.org/10.1109/TPAMI.1986.4767851

Deen, N. G., Willems, P., Sint Annaland, M. Van, Kuipers, J. A. M., Lammertink, R. G. H., Kemperman, A. J. B., … Van Der Meer, W. G. J. (2010). On image pre-processing for PIV of single-and two-phase flows over reflecting objects. *Experiments in Fluids*, *49*(2), 525–530. https://doi.org/10.1007/s00348-010-0827-y

Dussol, D., Druault, P., Mallat, B., Delacroix, S., & Germain, G. (2016). Automatic dynamic mask extraction for PIV images containing an unsteady interface, bubbles, and a moving structure. *Comptes Rendus - Mecanique*, *344*(7), 464–478. https://doi.org/10.1016/j.crme.2016.03.005

Gui, L., & Merzkirch, W. (1998). Generating arbitrarily sized interrogation windows for correlation-based analysis of particle image velocimetry recordings. *Experiments in Fluids*, *24*(1), 66–69. https://doi.org/10.1007/s003480050151

Huang, H. T., Fiedler, H. E., & Wang, J. J. (1993a). Limitation and improvement of PIV - Part I: Limitation of conventional techniques due to deformation of particle image patterns. *Experiments in Fluids*, *15*(3), 168–174. https://doi.org/10.1007/BF00189883

Huang, H. T., Fiedler, H. E., & Wang, J. J. (1993b). Limitation and improvement of PIV - Part II: Particle image distortion, a novel technique. *Experiments in Fluids*, *15*(4–5), 263–273. https://doi.org/10.1007/BF00223404

Jambunathan, K., Ju, X. Y., Dobbins, B. N., & Ashforth-Frost, S. (1999). An improved cross correlation technique for particle image velocimetry. *Measurement Science and Technology*, *6*(5), 507–514. https://doi.org/10.1088/0957-0233/6/5/012

Masullo, A., & Theunissen, R. (2017). Automated mask generation for PIV image analysis based on pixel intensity statistics. *Experiments in Fluids*, *58*(6), 1–11. https://doi.org/10.1007/s00348-017-2357-3

Masullo, A., & Theunissen, R. (2017). On the applicability of numerical image mapping for PIV image analysis near curved interfaces. *Measurement Science and Technology*, *28*(7). https://doi.org/10.1088/1361-6501/aa6c8f

Meinhart, C. D., Wereley, S. T., & Santiago, J. G. (1999). PIV measurements of a microchannel flow. *Experiments in Fluids*, *27*(5), 414–419. https://doi.org/10.1007/s003480050366

Mendez, M. A., Raiola, M., Masullo, A., Discetti, S., Ianiro, A., Theunissen, R., & Buchlin, J. M. (2017). POD-based background removal for particle image velocimetry. *Experimental Thermal and Fluid Science*, *80*, 181–192. https://doi.org/10.1016/j.expthermflusci.2016.08.021

Munson, B. R., Okiishi, T. H., Huebsch, W. W., & Rothmayer, A. P. (2013). *Fundamentals of Fluid Mechanics* (7th ed.). Wiley.

NASA, & Rumsey, C. (2018). 2D NACA 0012 Airfoil Validation Case. Retrieved April 24, 2018, from https://turbmodels.larc.nasa.gov/naca0012_val.html

Nguyen, T. D., Wells, J. C., & Nguyen, C. V. (2012). Velocity measurement of near-wall flow over inclined and curved boundaries by extended interfacial particle image velocimetry. *Flow Measurement and Instrumentation*, *23*(1), 33–39. https://doi.org/10.1016/j.flowmeasinst.2011.12.006

Nguyen, C. V., Nguyen, T. D., Wells, J. C., & Nakayama, A. (2010). Interfacial PIV to resolve

flows in the vicinity of curved surfaces. *Experiments in Fluids*, *48*(4), 577–587. https://doi.org/10.1007/s00348-010-0824-1

Nogueira, J., & Lecuona, a. (2004). The local field correction advanced PIV algorithm. *Particle Image Velocimetry …*, (1999). Retrieved from http://link.springer.com/chapter/10.1007/978-3-642-18795-7_7

Park, J., Im, S., Sung, H. J., & Park, J. S. (2015). PIV measurements of flow around an arbitrarily moving free surface. *Experiments in Fluids*, *56*(3). https://doi.org/10.1007/s00348-015-1920-z

Paterna, E., Moonen, P., Dorer, V., & Carmeliet, J. (2013). Mitigation of surface reflection in PIV measurements. *Measurement Science and Technology*, *24*(5). https://doi.org/10.1088/0957-0233/24/5/057003

Ronneberger, O., Raffel, M., & Kompenhans, J. (1998). Advanced evaluation algorithms for standard and dual plane particle image velocimetry. *Proceedings of the 9th International Symposium on Applied Laser Techniques to Fluid Mechanics*, 13–16. Retrieved from http://lmb.informatik.uni-freiburg.de/Publications/1998/Ron98a/1998_Ronneberger_Dual_Plane_Particle_Image_Velocimetry.pdf

Scarano, F., & Riethmuller, M. L. (1999). Iterative multigrid approach in PIV image processing with discrete window offset. *Experiments in Fluids*, *26*(6), 513–523. https://doi.org/10.1007/s003480050318

Theunissen, R., Scarano, F., & Riethmuller, M. L. (2008). On improvement of PIV image interrogation near stationary interfaces. *Experiments in Fluids*, *45*(4), 557–572. https://doi.org/10.1007/s00348-008-0481-9

Wenguo, W., Fan, W., Liao, Gu., & Qin, J. (2001). An improved cross-correlation method for (digital) particle image velocimetry. *ACTA MECHANICA SINICA(English Series)*, *17*(4), 332–339.

Westerweel, J. (1994). Efficient detection of spurious vectors in particle image velocimetry data. *Experiments in Fluids*, *16*(3–4), 236–247. https://doi.org/10.1007/BF00206543